Failure analysis of GFRP single lap joints tailored with a combination of tough epoxy and hyperelastic adhesives

D.V. Srinivasan[a], V. Ravichandran[a], S. Idapalapati[a,b,*]

[a]*Rolls-Royce@NTU Corporate Laboratory, School of Mechanical and Aerospace Engineering, Nanyang Technological University, Singapore 639798, Singapore.*
[b]*Energy Research Institute@NTU, 1 CleanTech Loop, Singapore 637141, Singapore.*

Abstract

Fibre reinforced polymeric composites bonded with epoxy adhesives often fail ungraciously, manifesting fibre-tear failure due to the edge peel stresses. This research work proposes phenol formaldehyde-based hyperelastic adhesive (AF32), as a compliant adhesive for tailoring the single lap joints consisting of GFRP adherends and well-toughened epoxy adhesive (AF3109 and EA9696) joints. The failure strength of the AF3109 and EA9696 adhesive joints is increased by 51.64% and 24.25%, respectively by having 20% volume of compliant adhesive in the bond line. Finite element simulations with Exponential Drucker-Prager (EDP) and Marlow strain energy models are carried out to simulate the experimental load-displacement response. Different failure mechanisms and the influence of adhesive intermingling are revealed by the failure analysis. Finally, a failure mode map for the tailored adhesive joints is proposed in terms of normalised strength ratio and the normalised volume of the compliant adhesive.

Keywords: Tailoring; B. Adhesion; B. Strength; C. Finite element analysis; E. Joints.

* Corresponding author: S.Idapalapati
Email-address: msridhar@ntu.edu.sg

1 Introduction

Adhesively bonded composite joints are prominently used in original component manufacturing or repair of airframes, wind turbine blades and gas-turbine engine casings. The joint design can differ from simple single lap joints (SLJs) to scarf joints based on the loading requirements, cost and available facilities [1, 2]. Various joint design parameters not limited to adherend stiffness, adhesive type and constitutive behaviour, bond line length, bond line thickness and desired adherend-adhesive interface properties were studied by da Silva at al. [3], Tang et al. [4] and Banea et al. [5]. The parameters can be well-engineered to adhere the structural and hygro-thermal loading conditions. Among the different adhesive joints, SLJs are the most common, easy to fabricate and extensively investigated by the scientific community. Adams [6] discussed that the overlapping edges undergo a high concentration of shear and peel stresses due to the geometric and material discontinuities and out-of-plane bending caused by the load eccentricity. These stresses are detrimental to the composite adherends bonded with epoxy adhesives where the fibre-tear failure occurs due to inferior inter-laminar strength and it was studied by Fitton et al. [7] with variable modulus adhesive joints. Numerous techniques such as tapering the adherend ends, filleting and adhesive tailoring were reviewed by da Silva et al. [8] and Shang et al. [9] to reduce the edge stress concentration. Other strategies including increasing the through-thickness strength and tailoring the modulus of the composite adherends to withstand the peel stresses were attempted at the expense of manufacturability. Boss et al. [10] examined the tailoring of geometry and modulus of the single lap adhesive joints by means of varying the braided angle along the overlap length. In the adhesive tailoring technique, a compliant adhesive is cured at the overlapping edges and a stiff adhesive in the central region of the joint that reduces the edge peel stresses. Previous experimental studies on the tailored single lap adhesive joints have proved a promising improvement in the joint failure load. Fitton et al. [7] tailored the unidirectional carbon fibre reinforced polymeric (CFRP) composite-brittle adhesive joints using 20% ductile epoxy adhesive (Young's moduli ratio of 7.5). da Silva et al. [11] introduced silicon rubber strips for fabricating the steel DINC75 single lap joints bonded with a combination of brittle and ductile epoxies. Marques et al. [12] experimented with silicon and epoxy bi-adhesive joints for high-temperature applications: the tailored joints showed increase in strength at room temperature and 100°C than the pristine joints. Durudola et al. [13] reviewed the research work on the bi-adhesive joints and highlighted the challenges such as adhesive squeeze out, curing cycle of the tailored adhesives and common surface treatments. Kumar et al. [14] used 3D printed rigid polymer (VeroWhitePlus RGD835) adherends as well as tailored the adhesive joints with two different modulus adhesives having Young's modulus ratio of 2 and bond line thickness of 7 mm. The tailoring strategy improved the joint strength by more than 100%. Stapleton et al. [15] used a single adhesive system to tailor the single-strap adhesive joints in which functional materials such as glass beads were added at the edges for varying the modulus, resulted with 26.5% increase in the failure load.

The peel and shear stress distribution of the tailored adhesive joints were determined by several analytical and numerical models [16–19]. However, finite element (FE) analysis is an efficient and versatile tool to predict the material and geometric nonlinear behaviour of the adhesive joints. Galvez et al. [20] identified the effect of Young's modulus of bi-adhesives on the stress

singularity field (SSF) at the joint corners and showed 35.64% reduction in stress intensity. Cohesive zone models based on traction-seperation laws can be useful to analyse the adhesive-adherend interface failures of the adhesive joints [21]. Garcia et al. [22], Ozer et al.[23] and Xu [24] used Exponential Drugger-Pracker (EDP) model and Stuadt et al. [25] explored Marlow strain energy based hyperelastic model to analyse the epoxy and hyperelastic adhesives that experience isotropic plastic hardening and extensive strain, respectively.

However, these studies were limited to non-structural applications, paste adhesives, high bond line thicknesses, low Young's modulus ratio, brittle-ductile adhesive combinations and high stiffness adherends. To the best of authors knowledge, there is no published work demonstrating the tailoring characteristics of the hyperelastic adhesives combined with ductile epoxy film adhesives. This paper intends to examine the tailoring capability of acrylonitrile-butadiene rubber-modified phenolic formaldehyde adhesive, introduced at the GFRP adherend-epoxy adhesive joints by evaluating their single lap shear strength. The mechanical response and the stress state of the adhesive joints were simulated by FE models and a comprehensive failure analysis was carried out to map the failure modes with respect to the normalised strength ratio and the normalised volume of compliant adhesive.

2 Materials and manufacturing

Three different types of commercially available adhesives with trade names AF3109, EA9696 and AF32 were used in fabricating the bulk adhesive specimens for uniaxial tensile testing as well as bonding the GFRP adherends. AF3109 is a two component (epoxy + dicyandiamide) nylon scrim supported epoxy film adhesive procured from 3M®. Hysol® EA9696 is an unsupported epoxy film adhesive providing high toughness and excellent environmental resistance that finds application in composite to metal bonding. AF32 is a phenol-formaldehyde based adhesive that contains 40% to 70% by weight of acrylonitrile-butadiene rubber particles, procured from 3M® [26]. The chemical compositions are withheld by the manufacturers due to confidentiality. The mechanical properties and single lap shear or design strength of the adhesives from the manufacturer's technical data sheets (TDS) are listed in Table 1. It should be noted that AF3109 and EA9696 adhesives are considered as stiff adhesives because their tensile Young's moduli are approximately 100 and 70 times that of AF32 adhesive. Relatively, AF3109 is a high modulus, low shear strength adhesive as compared to EA9696 adhesive.

Table 1. Adhesive material properties from the technical data sheets [27-29].

Adhesive name	Young's modulus (GPa)	Tensile strength (MPa)	Single lap shear strength, τ_s (MPa)
AF3109	2.69	59.6	38.6
EA9696	1.91	47.2	42.9
AF32	0.0267	15.8	17.2

For the bulk adhesive tensile testing, the film adhesive layers were degassed for every 2 layers and cured inside a vacuum-bagged mould. The adhesives were cured at 150°C temperature, over a period of 60 minutes, where the heating and cooling rate was maintained at 3°C/min,

under a pressure of 520 kPa and 140 kPa vacuum. The cured adhesive plates were computer numerical control (CNC) machined into type IV dog bone shapes (Figure 1a), as recommended by ASTM standard D638 [30]. For the practical purpose, all three adhesives were cured using the same curing cycle for tailoring the GFRP adhesive joints and a slight reduction in the single lap shear strength is expected as further elaborated in section 4.5. For example, the hyperelastic adhesive softening in the temperature range of 82°C to 99°C initiates chemical curing in between 93°C to 132°C and forms a low strength gel. Further maintaining optimal temperature (177°C for 120 minutes) a high degree of cure and shear strength can be achieved [29].

Unidirectional glass fibre reinforced epoxy prepregs G17500/6509/33% procured from Weihai GuangWei Composites Co., Ltd were used to fabricate the GFRP adherends. In total, 25 layers of prepreg were vacuum degassed for every 3 layers and stacked unidirectionally to achieve a post-cure thickness of 2.75 mm. The uncured laminate was vacuum-bagged and cured in an autoclave at a dwell temperature of 150°C for 120 minutes under 340 kPa pressure and 76 kPa vacuum. The mechanical properties of the unidirectional composite as measured earlier by Rajaneesh et al. [31] are listed in

Table 2. The cured laminate of 25 mm x 145 mm was machined using the water-assisted rotary diamond cutter for fabricating the bonded joints. Similar adherend geometry was employed by Özer and Öz [23].

Table 2. Material properties of the GFRP adherend [31].

GFRP adherend properties	Values
Density (kg/m^3)	2200
Tensile moduli (GPa) E_{11}, E_{22}	46, 13
Shear moduli (GPa) G_{12}, G_{13}, G_{23}	7.0, 6.5, 4.48
Poisson's ratio $\nu_{12}, \nu_{13}, \nu_{23}$	0.26, 0.074, 0.44

Before bonding, the GFRP adherend bonding surface was dry-grit blasted for 25 ± 5 s at 200 kPa with 120 µm white alumina powder, which gave a surface roughness (R_a) of 3.07 µm and water contact angle of 48˚, by removing a thin layer of the epoxy matrix. After cleaning with deionized water, the samples were dried inside an air circulating oven for 30 minutes at 60°C and degreased with acetone before applying the primer. An acetone-epoxy primer was prepared in-house and coated on the adherend surface to promote good adhesion, especially with the hyperelastic adhesives. The acetone in the primer coating was removed by drying the adherends in a convection oven for 60 minutes at 80°C.

Following the surface preparation, the pristine adhesive joints (S1, S2 and C1, see Table 3 for nomenclature) were fabricated with a single layer of adhesive (25 mm x 50 mm) whereas the tailored adhesive joints were designed with two different proportions of compliant adhesive (l_c) for the total bond length (l_b), as given in Table 3. A metallic shim of 0.2 mm thickness was placed underneath the top adherend to control the bond line thickness. Detailed joint fabrication process is included in section S1 of supplementary information. The choice of l_c relative to l_s was selected randomly as 5 mm and 12.5 mm because (a) it is difficult to fabricate the joints

having l_c smaller than 5 mm due to adhesives intermingling and squeeze-out and (b) l_c greater than 12.5 mm would require more complaint adhesive and may reduce the joint strength.

Table 3. Design details of the pristine and tailored adhesive joints and l_b is 50 mm.

S.No	Design	Stiff adhesive	Compliant adhesive	Proportion $\left(\frac{2l_c}{l_b}\right)$	Description
1	S1	AF3109	-	0	Prisitine AF3109 epoxy SLJ
2	S2	EA9696	-	0	Pristine EA9696 epoxy SLJ
3	C1	-	AF32	1	Pristine AF32 hyperelastic SLJ
4	AA1	AF3109	AF32	0.5	AF3109 based tailored SLJ
5	AA2	AF3109	AF32	0.2	
6	EA1	EA9696	AF32	0.5	EA9696 based tailored SLJ
7	EA2	EA9696	AF32	0.2	

After bonding, the alignment tabs made up of M21 woven GFRP laminate, having a dimension of 25 mm x 25 mm were bonded using a quick fix liquid adhesive (industrial-grade SG 110-2). The total thickness of ~2.95 mm ensured that the line of applied force passes through the bond line. Single-element TML strain gauges, GFLA-3-350-70 were bonded on either side of the GFRP adherend, at a distance of 5 mm from the edge of the overlap length, to measure the localized strains along the axis of tensile loading. Figure 1b depicts the dimensions and strain gauge locations of a typical tailored adhesive joint design with stiff adhesive of length, l_s, placed in between the outer compliant adhesive of length, l_c.

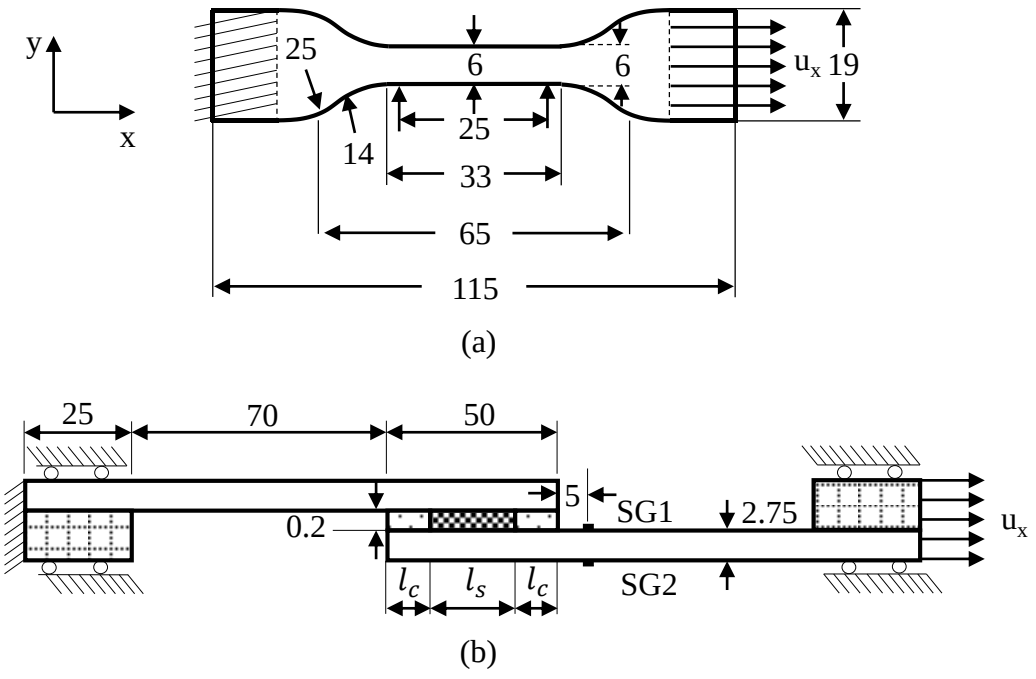

Figure 1. Geometric details of samples and FE models with representative boundary and loading conditions. All dimensions are in millimeters: (a) type IV dog bone shape bulk

adhesive of 3 mm thickness and (b) single lap adhesive joint. All the samples have total bond length (l_b) of 50 mm and width of 25 mm. l_c value is either 5 mm or 12.5 mm.

3 Experimental and numerical methods

The uniaxial tensile testing of bulk adhesives for developing the EDP and Marlow material models and single lap shear testing to assess the tailoring effect were a part of the experimental investigation. Commercial finite element software, ABAQUS® standard was used to simulate the mechanical response of bulk adhesives and adhesive joints and carry out the detailed stress analysis under uniaxial tensile loading. Figure 2 shows the flow chart of the experimental and numerical approaches employed in the current investigation.

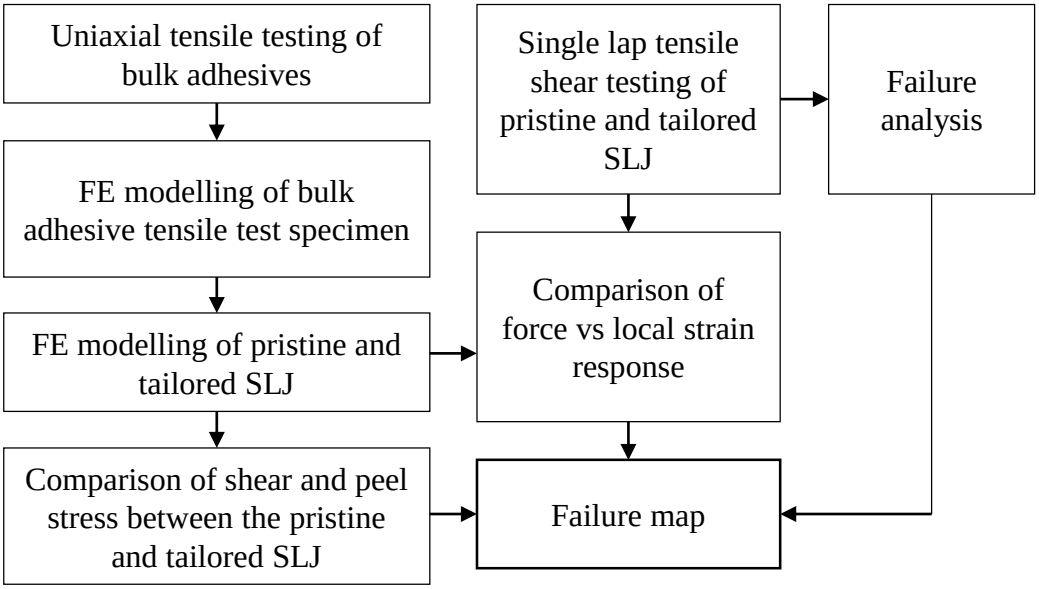

Figure 2. Experimental and numerical methodology for tailoring the adhesive joints.

In industrial applications, the actual-load strain response of the adhesive joints may differ from the narrow single lap test samples tested in a controlled enviroment. In certain cases, other tests such as push-out tests can be carried out to sufficiently characterize the adhesives [32].

3.1 Tensile testing of the bulk adhesives and adhesive joints

The uniaxial tensile testing of the bulk adhesive was performed under displacement control, at 1 mm/min, using a 10 kN Shimadzu Universal Testing Machine (UTM) equipped with an in-built video extensometer with a gauge length of 25 mm and elongation range of 200%. The tensile force and strain (both longitudinal and lateral) measured by the load cell and video extensometer were used to calculate Young's modulus, Poisson's ratio, yield strength and extended hardening values.

An Instron (UTM having a load cell capacity of 50 kN was used to conduct the tensile testing of pristine and tailored adhesive joints at a displacement loading rate of 2 mm/min. The failure load was measured by the load cell whereas the displacement was recorded through the crosshead displacement. The ultimate average shear strength of the adhesive joints (τ_t) under tensile loading was obtained by $\tau_t = P_{max}/A$, where P_{max} is the maximum load at failure and

A is the adhesive bond area (1250 mm^2). The soldered wires of the strain gauges (SG1 and SG2) were connected to the TDS-303® data logger for acquiring the localized strain at a frequency of 1 Hz. All the tests were conducted at room temperature of 25 ± 2˚C and a relative humidity of 50 ± 5%.

3.2 Finite element modelling of the bulk adhesives and adhesive joints

Finite element (FE) analysis was carried out for the following two categories: (a) a dog bone shape adhesive model having the geometric details of ASTM standard D638-type IV, to verify the applicability of EDP and Marlow models and (b) the pristine and tailored SLJ model to analyse the tailoring effect on the tensile load-displacement response. No failure criteria were applied to the adhesives and GFRP adherend.

The bulk adhesive model was discretized using 2360 CPS4R elements (4-node bilinear plane stress quadrilateral, reduced integration, hourglass control) and applied with fixed and displacement boundary conditions at both ends, respectively (Figure 1a). A displacement of 2.5 mm along the longitudinal direction (u_x) was applied to the AF3109 and EA9696 adhesive models, whereas the AF32 adhesive model was loaded with 50 mm to capture the large strain response. The non-linear geometry option was enabled to accommodate the adhesive hardening and large strain-displacement relation. The von Mises effective stress and logarithmic strain along the longitudinal direction were taken from the central element (Refer Figure S2 of supplementary information)

The schematic diagram in Figure 1b illustrates the dimensions and boundary conditions used in the numerical modelling of a tailored adhesive joint FE model. The clamping and displacement loading conditions were simulated as in the single lap tensile shear testing. All the pristine and tailored adhesive joints models were assumed in-plane strain condition, as the width (25 mm) of the adhesive joints was higher than the thickness (2.75 mm). The GFRP adherend, AF3109 adhesive, EA9696 adhesive and alignment tabs were meshed with CPE4R (A 4-node bilinear plane strain quadrilateral, reduced integration, hourglass control) elements. The overlapping region of the GFRP adherend was discretized with 15 elements, through-thickness direction with a double bias ratio of 15. The top and bottom surface element size was 0.033 mm x 0.037 mm that increased to 0.033 mm x 0.55 mm in the middle. The structural mesh of AF32 adhesive region had CPE4RH (4-node bilinear plane strain quadrilateral, hybrid, constant pressure, reduced integration, hourglass control) hybrid elements to integrate the poor compressibility of the hyperelastic adhesives. The entire adhesive region has six through-thickness elements of 0.033 mm x 0.033 mm (Refer Figure S3 of supplementary information)

3.3 Adhesive material models for FE simulations

The adhesive joints with high toughness adhesives and high peel stresses could not be modelled with simple elastic behaviour. The elastic material properties of adhesives measured through uniaxial tensile testing were given as input to the FE models (Table 4).

Table 4. Elastic material properties of the adhesives used in FE modelling.

Adhesive name	Young's modulus (GPa)	Poisson's ratio
AF3109	2.25	0.43*
EA9696	1.63	0.43
AF32	-	0.49

*Reference [33].

Exponential Drucker-Prager (EDP) model was shown to represent the pressure-dependent yield behaviour of ductile epoxy adhesives and the details are summarised in Appendix. Smith [33] and Mohapatra et al. [34], characterised the EDP parameters of EA9696 adhesive and analysed various joint configurations including single lap shear, wide lap shear, thick adherend lap shear and scarf joints. The EA9696 adhesive joint behaviour was well predicted by the EDP models with extended hardening material properties as compared to von Mises yield behaviour. The current study uses the same *a, b* and dilatation angle (ψ) values to reasonably predict the behaviour of epoxy adhesives EA9696 and AF3109, refer Table 5. The extended hardening values for the model were extracted from the uniaxial tensile testing and listed in Table S1 and Table S2 of supplementary information.

Table 5. EDP paramaters for the epoxy adhesives AF3109 and EA9696 [33].

EDP parameters	AF3109 and EA9696 adhesives
a	0.11603019 MPa^{-1}
b	2
Dilation angle	3.5º
Flow potential eccentricity	0.1

The constitutive behaviour of the hyperelastic adhesive, AF32 is governed by models such as Ogden, Mooney-Rivlin and Marlow and these can be calibrated against a combination of properties measured via uniaxial tensile, biaxial tensile, plane (pure shear) and simple shear tests. In this study, the Marlow model was employed which requires nominal stress and strain values which were directly imported to ABAQUS® from the uniaxial tensile test measurements.

4 Results and discussion

The experimental and numerical results of the bulk adhesives and adhesive joints along with failure mode analysis are presented in the following subsections.

4.1 Validation of the bulk adhesive tensile behaviour

The measured experimental and simulated numerical true stress versus true strain response of the bulk adhesives AF3109 and EA9696 are shown in Figure 3a. The initial linear elastic response of the stiff adhesives AF3109 and EA9696 was described by the tensile modulus, being the calculated values using 0.2% yield criteria were 2.27 ± 0.95 GPa and 1.64 ± 0.02 GPa, respectively. After deforming to a maximum strain of approximately 0.0365 and 0.1372,

the AF3019 and EA9696 were failed at the ultimate tensile stress of 59.72 ± 0.95 MPa and 48.3 ± 2.7 MPa, respectively. Similar material behaviour was well-predicted by the EDP model used in the FE analysis. Figure 3b reveals the hyperelastic behaviour of AF32 adhesive and the final failure could not be measured due to constraints in the gauge length of the video extensometer. However, the elastic-plastic response captured to a large strain of 75% was reproduced by the Marlow model.

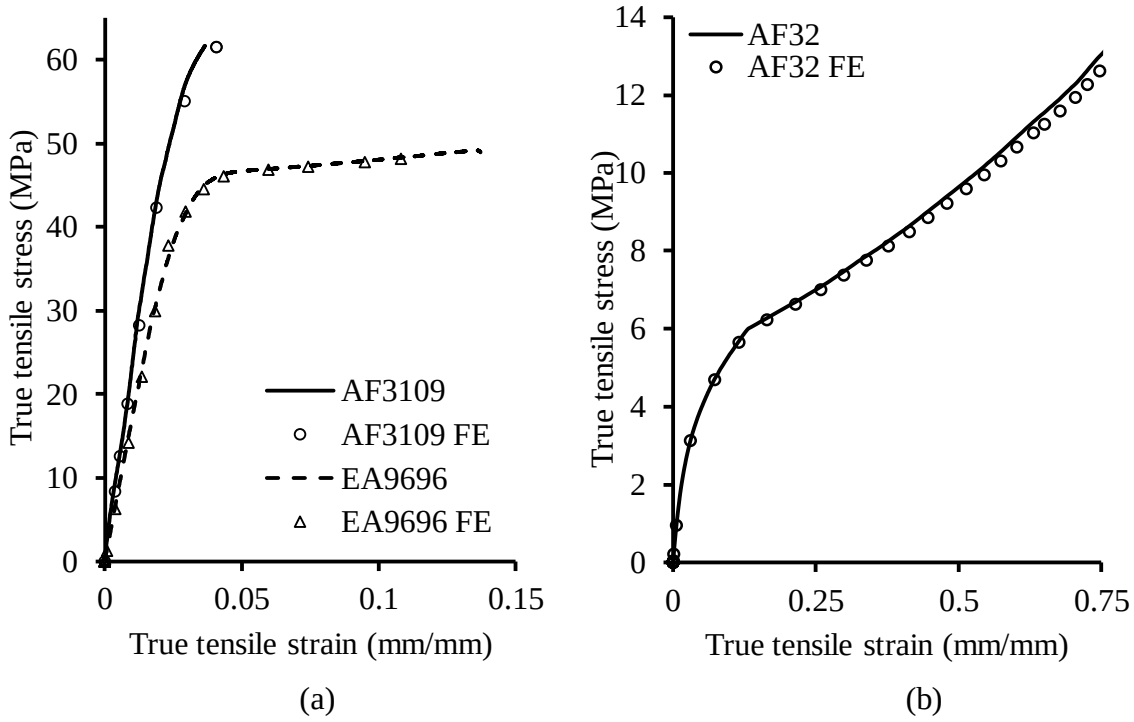

Figure 3. Uniaxial tensile stress versus strain response of the bulk adhesives: (a) AF3019 and EA9696, stiff adhesives and (b) AF32, compliant adhesive. FE denotes the results obtained from the finite element analysis.

4.2 Single lap shear strength of the tailored adhesive joints

The tensile force and displacement response of the pristine adhesive joints (S1:AF3109 and C1:AF32) and the AF3109 based tailored joints (AA1and AA2) were depicted in Figure 4a. Bonded joints with stiff adhesive have shown initial non-linear behaviour until around 6 kN, followed by a linear response till catastrophic failure. Whereas the pristine joints with compliant AF32 adhesive had shown non-linear response until the final failure at 16.44 kN load. The tailored adhesive joints were failed at an extended peak load of 28.64 kN and 36.6 kN that were 18.63% and 51.64% higher than the AF3109 adhesive joint (S1). Figure 4b compares the tensile force versus cross-head displacement response of the pristine adhesive joints (S2:EA9696 and C1:AF32) and EA9696 based tailored joints (EA1 and EA2). The S2 adhesive joints were failed at a maximum tensile load of 26.62 ± 1.36 kN whereas the EA1 and EA2 tailored joints were subjected to an average failure load of 24.62 ± 0.18 kN and 33.08 ± 1.19 kN, respectively. Surprisingly, the failure displacement of the stiff EA9696 adhesive joint, S2 was 1.15 times higher than the compliant adhesive joint, C1 because EA9696 adhesives can be subjected to more shear loading than AF32 adhesives (refer the single lap shear strength

data from Table 1). It should be noted that the SLJ (C1) behaviour was not expected as the bulk adhesive (AF32) due to the adherend boundary constraints.

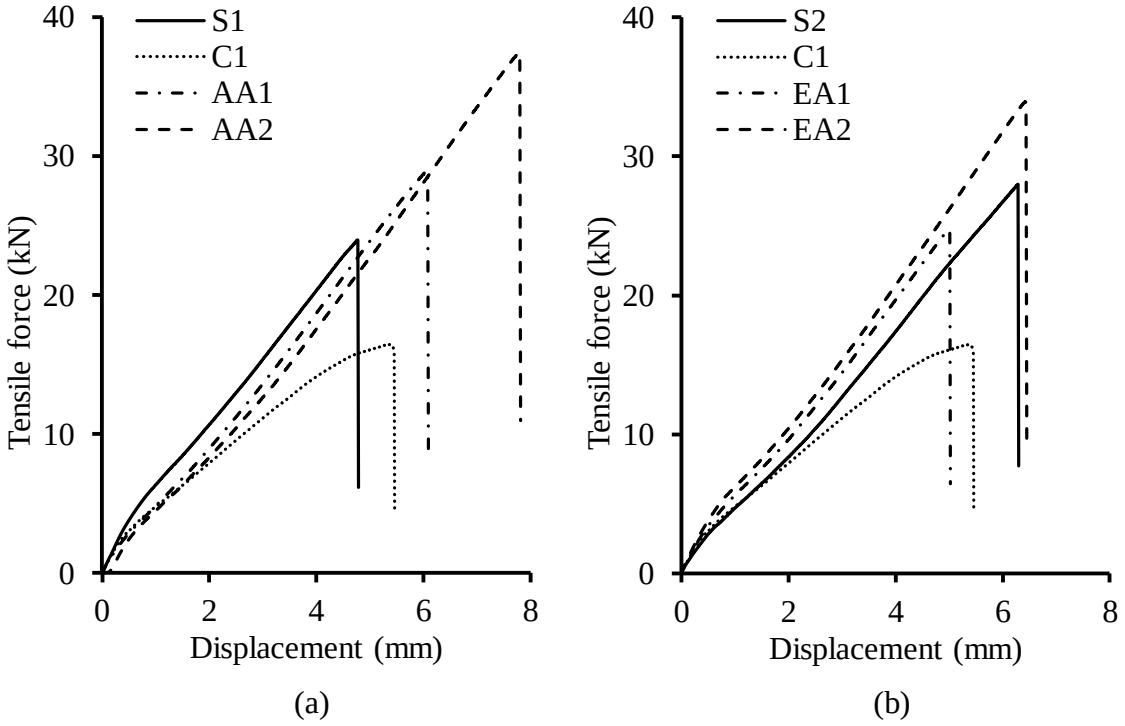

Figure 4. Tensile force versus cross-head displacement response of SLJs (a) AF3109-AF32 based joints and (b) EA9696-AF32 based joints.

The area under the load-displacement curves is a measure of the fracture energy and it is illustrated as a bar chart in Figure 5 for all the tested joints, along with the in-plane global stiffness, a slope of the linear portion of load-displacement response. The energy absorption of the AA1 and AA2 tailored joints were 43% and 115% higher than the underlying pristine joint, S1. In the case of the EA9696 based tailored joints (EA1 and EA2), the energy absorption was decreased by 21% and increased by 34.1%, respectively, as compared with the pristine joint, S2.

The stiffness of stiff adhesive joints (S1 and S2) were 1.15 and 1.12 times of the compliant adhesive joint (C1), respectively. Although the ultra-low modulus, hyperelastic adhesive was used for the tailoring, no reduction in joint stiffness was observed. Kumar et al. [35] showed that the in-plane global stiffness of the bi-adhesive joints was not significantly (< 0.5%) reduced by introducing the compliant adhesives through an analytical model. Within experimental scatter, there was no significant change in the in-plane global stiffness of the tailored joints comprising the AF3109 adhesive, whereas a maximum increment of 18.8% was observed with EA9696 based tailored joints (EA2). The increase in stiffness could be attributed to the reduction in edge shear and peel stresses and the following failure modes.

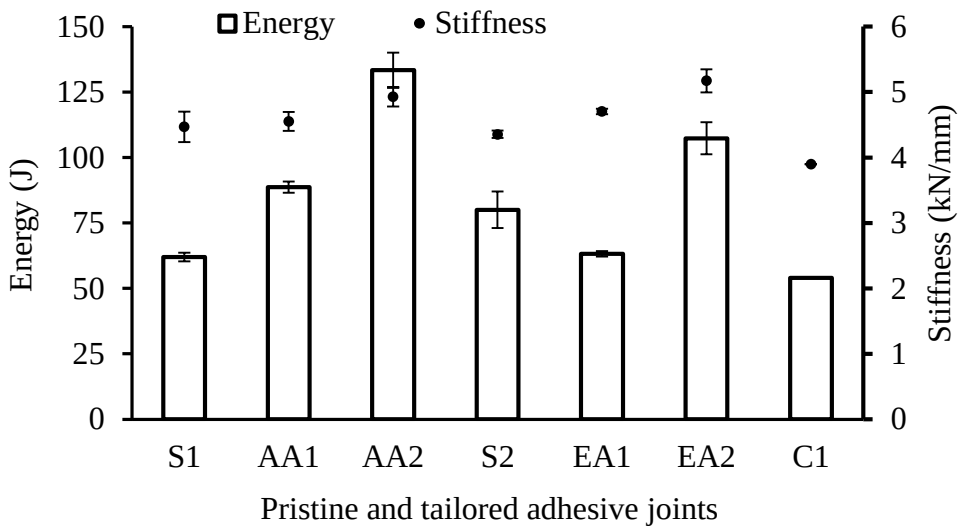

Figure 5. Energy and in-plane global stiffness of the pristine and tailored adhesive joints determined from the single lap shear testing.

The experimentally measured tensile response of the pristine adhesive joints (S1:AF3109 and C1:AF32) and the AF3109 based tailored joints (AA1 and AA2) with the corresponding FE simulations were depicted in Figure 6. The local strain of the GFRP adherend, near the bonded surface measured by the strain gauge SG1 was plotted with solid lines, whereas the outer surface strain recorded by the strain gauge SG2 as dashed lines. Similarly, the corresponding FE simulation responses are denoted as FE1 and FE2, indicated by filled and unfilled markers, respectively which compares well with the experimental measurements. Initially, the GFRP adhesive joints were subjected to a small amount of bending moment, up to 6 kN, as revealed by the presence of tensile and compressive strain at either side of the adherend. The slight deviation between the numerical and experimental curves of the tailored joints was generally attributed to manufacturing deficiencies such as adhesive intermingling and unsymmetrical compliant adhesive proportion as discussed further in section 4.3. A strain gauge, SG2 in the AA2 joints was slightly mis-aligned by about 10^{o}, relative to the axial direction. Due to this experimental error, the measured strain value was higher than the numerical prediction because the modulus of unidirectional composite is lower along the off-axis direction.

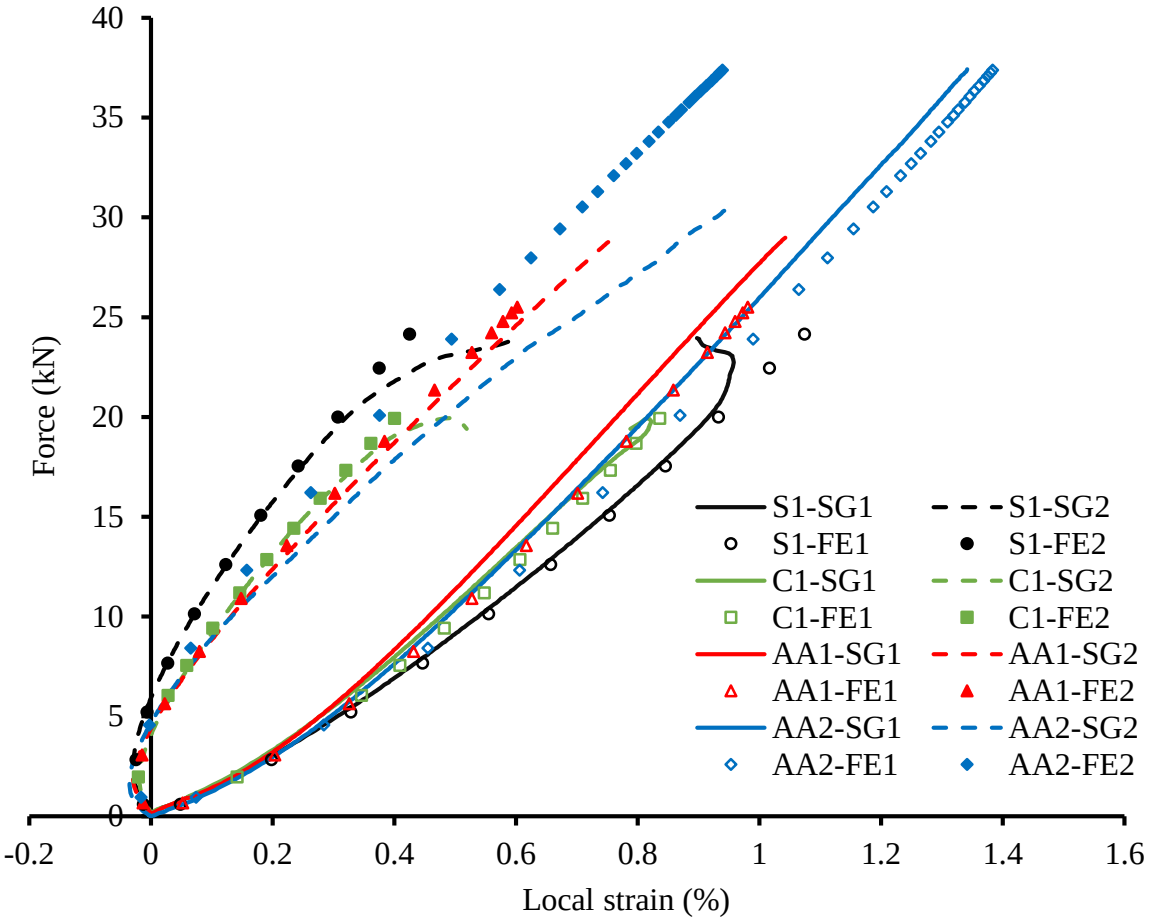

Figure 6. Force versus local strain response curves of the pristine and AF3109 based tailored joints. SG and FE refers to the strain gauage and finite FE simulation values, respectively.

4.3 Failure analysis

The failure modes of the tested adhesive joints and their corresponding percentages were analysed as per ASTM D5573-99(2019) [36] and the failure surface images are presented in Table 6. The pristine adhesive joints, S1 and S2 were shown fibre-tear failure (FT) whereas the compliant joint exhibited thin-layer cohesive failure (TLC). The tailored adhesive joints AA1 and EA1 showed a mixed failure: a combination of TLC and cohesive (COH) failure in the compliant and stiff adhesive regions respectively. The tailored joints AA2 and EA2 were also revealed a combined failure of TLC, COH and light-fibre-tear (LFT) failure.

Table 6. Failure surface and major failure modes of the tested adhesive joints. All the images correspond to the total bond length of 50 mm. Abbreviations FT, COH, TLC and LFT refer to fibre-tear, cohesive, thin-layer cohesive and light-fibre-tear failure modes. The failure mode percentages are given in the brackets. The epoxy and hyperelastic adhesive transition region is highlighted in the tailored SLJs.

S1: FT(90%), COH(10%)	S2: FT(96%), COH(4%)	C1: TLC(98%), LFT(2%)
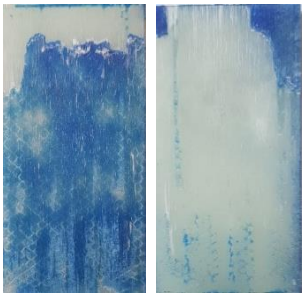	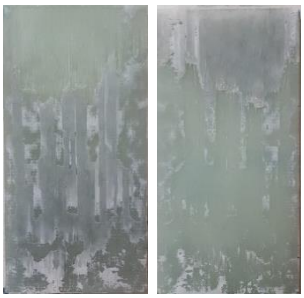	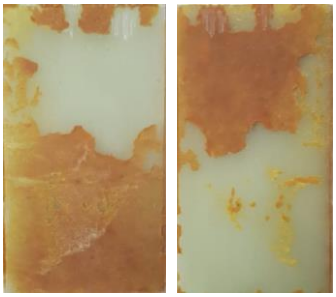

AA1: COH(50%), TLC(50%)	AA2: COH(47%), LFT(33%), TLC(20%)
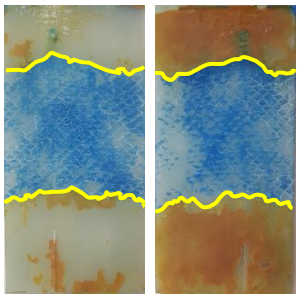	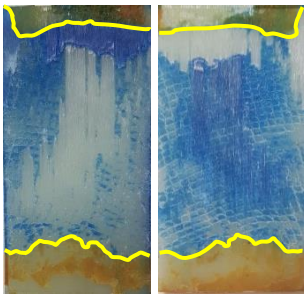

EA1: CF(50%), TLC(50%)	EA2: COH(64%), LFT(16%), TLC(20%)
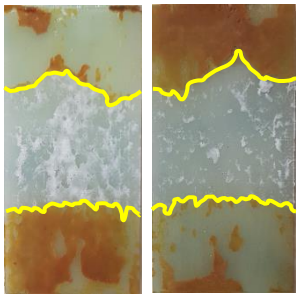	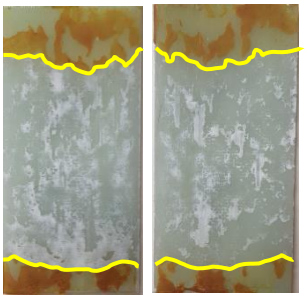

The microscopic images of the AA1 and AA2 failure surface in Figure 7 shows the intermingling of the AF3109 and AF32 adhesives having disparity in strength and stiffness, also known as the transition region. The AF3109 adhesive was flown into the AF32 adhesive region due to: (a) the mismatch in stiff and compliant adhesive viscosities while curing and (b) the potential energy imbalance due to small inclination of the curing setup that resulted in unsymmetrical compliant adhesive proportion (l_c). The manufacturing challenges such as adhesive squeeze out and curing setup were outlined by Durodola [13]. Another important

aspect of this study was investigating the implications of manufacturing deficiencies on the joint performance and the failure mechanisms.

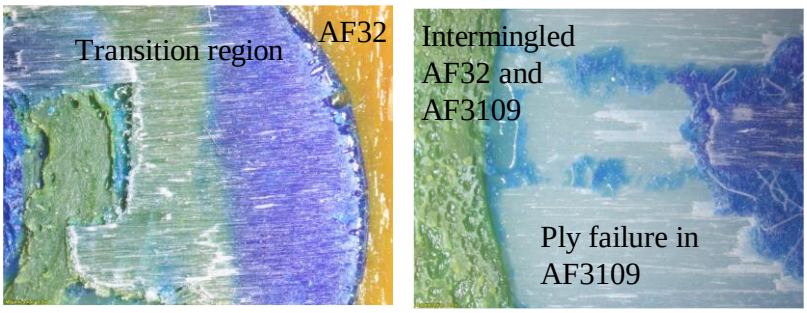

a b

Figure 7. Failure surface near the transition region: (a) fibre-tear failure originating from the stiff adhesive (AF3109) region in the AA1 joint and (b) initiation of the fibre-tear failure only at AF3109 region of the AA2 joint.

Figure 8a depicts the fibre-tear failure of untailored composite SLJs due to high edge peel stresses. The delamination initiated at the both adherends would propagate to the outer edges and finally fracture in the middle. However, the complex fracture paths were revealed by the tailored adhesive joints having intermingled stiff and compliant adhesives as shown in Figure 8b, 8c and 8d.

Figure 8b shows the fracture path of the AA1 joint (50% AF3109 and 50% AF32) and the unsymmetrical compliant adhesive length (l_c) due to the curing process. The four different regions from left to right are: (a) pure AF32 compliant adhesive region erless than 12.5 mm- the crack was in the adhesive bond line,showing TLC failure (b) transition region- the delamination in the first ply of the composite adherend at an insignificant length could not continue in the laminate pliesand hence the crack kinks back to the former region with FT failure, (c) stiff AF3109 adhesive region- the crack was seen in the adhesive bond line resulting in complete cohesive failure exposing the nylon scrims on the failure surface of both the adherends. In this region, the AF3109 adhesive was subjected to the maximum shear stress, a clear indication of attaining its full material strength and (d) pure AF32 compliant adhesive region greater than 12.5 mm- the crack was still presented in the adhesive bond line, revealing TLC failure.

Figure 8c shows the crack path of the AA2 joint containing 20% AF32 adhesive. The crack path was observed in both edges of the pure AF32 compliant adhesive. However, the stiff adhesive region was observed with a combined adhesive cohesive and fibre-tear failure of composite that was not uniform across the width. So this l_c can be considered as a critical value where the peel dominated failure changes into shear dominanted failure.

Figure 8d shows the crack path selection in the EA2 joint having 20% AF32 adhesive. Similar to the AA2 tailored joint, the pure AF32 adhesive region were exhibited TLC in both edges and the stiff EA9696 adhesive region was observed with a combined COH and LFT failure. In spite of having the adhesives intermingling with unsymmetrical l_c, the reliability and

repeatability of the tailored joint seem higher, referring to the experimental scatter of the joint failure strength (refer to Table S3 in the supplementary information). A maximum of 3.6% scatter in joint strength was noticed in the EA2 joints.

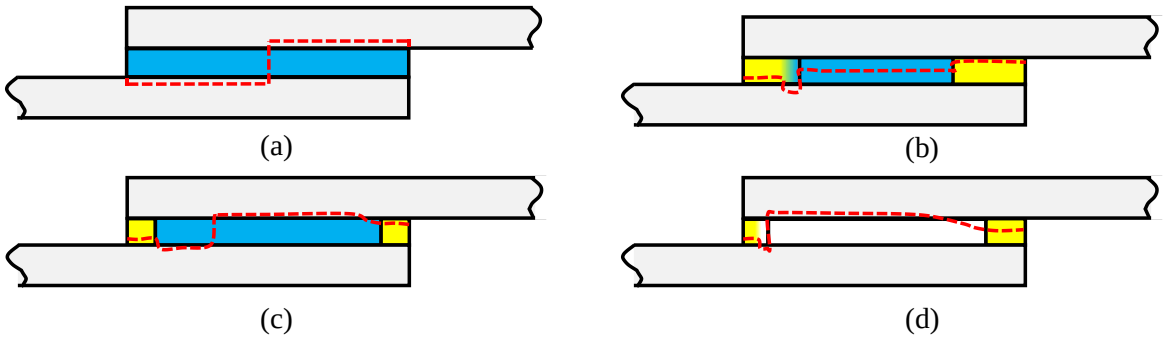

Figure 8. Competing fracture paths in SLJs under the tensile load: (a) conventional SLJ having composite first-ply or fibre-tear failure (b) insignificant ply failure in the transition region at AA1, (c) fibre-tear failure originating in the transition region of AA2 and (d) multiple failure modes in EA2. Refer to Table 3 for notations.

4.4 Finite element analysis of the tailored adhesive joints

Figure 9a shows the GFRP adherends-adhesive interfacial shear strength calculated on the bottom adhesive surface over the 50 mm bond length. Maximum shear stress values of 36.34 MPa, 16.52 MPa, 36.43 MPa and 36.48 MPa were ascertained in the adhesive joints S1, C1, AA1 and AA2, respectively at the instant of joint failure load. It is to be noted that the shear and peel stress distribution for the pristine joints follow the modified Goland and Reissner (G-R) models [37].

In the pristine adhesive joints (S1 and C1), the stresses are concentrated at the free edges and reduced to a minimum across the overall length of the bond line. Unlike the pristine joints, the minimum shear in the tailored joints was observed at the joint corner edges due to the presence of hyperelastic adhesive. Severe deformation of AF32 adhesive in the overlapping edges of the tailored joints was observed and represented by the presence of positive shear stress. The AA1 exhibiting uniform shear stress distribution in the middle was due to yielding of the AF3019 adhesive that can be confirmed by the cohesive failure surface. In this context, a small valley in the shear stress distribution plot of the AA2 adhesive joint was identified, implicating the yielding had not yet occurred.

Figure 9b shows the peak peel stress of 54.93 MPa and 21.51 MPa was observed at the overlapping edges of the pristine joints, S1 and C1. The edge peel stresses of the tailored joints AA1 and AA2 were reduced by 77.83% and 66.17%, respectively. Whereas, the tensile peak peel stresses of 53.64 MPa and 54.13 MPa was observed at the stiff and compliant adhesive transition region of the respective tailored joints. The observed stress discontinuity in the transition region was due to the varying Young's modulus with displacement or strain continuity. The other transition region in the bond line was regarded with compressive peel stress in contrast to the pristine joints.

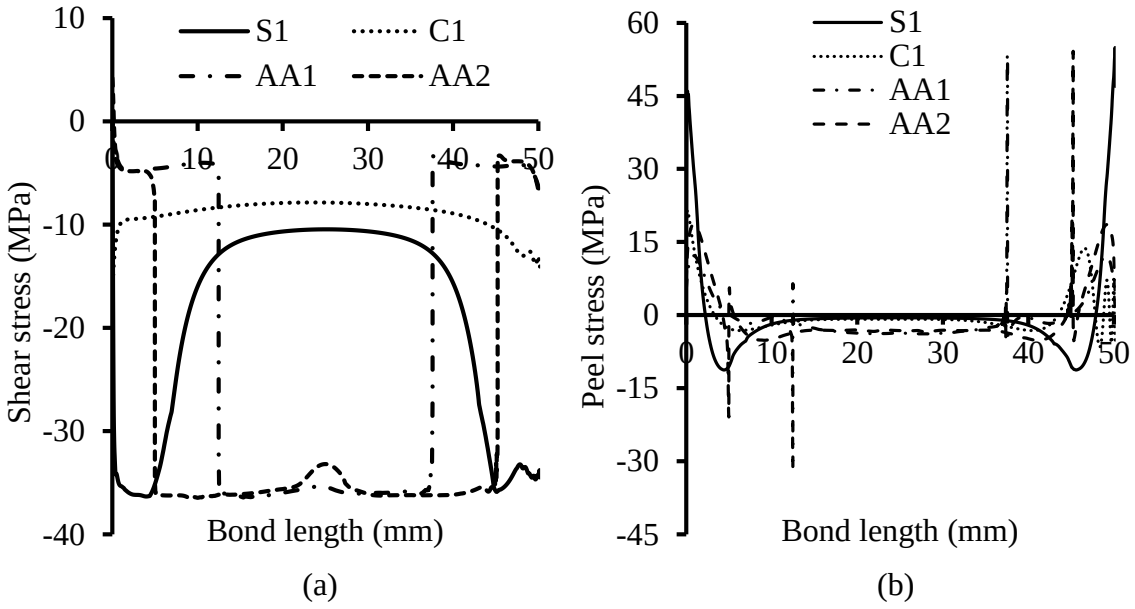

Figure 9. Stress distribution at the bottom adhesive-adherend interface across the bond the length when the displacement corresponding to the failure force is applied: (a) shear stress and (b) peel stress.

4.5 Failure mode map for the tailored adhesive joints

Herein through proper surface treatment to the GFRP adherends, the adhesive failure was suppressed, leaving either composite adherend fibre-tear failure or cohesive failure. A failure mode map was obtained in Figure 10 by plotting the normalised failure strength (ratio of the joint strength (τ_t) with stiff adhesive design strength (τ_s)) against the normalised compliant adhesive volume ($2l_c/l_b$). Using the rule of mixtures (RoM), a upper bound to the tailored adhesive joint strength can be expressed in terms of stiff and compliant adhesive design strength (τ_c) as,

$$\tau_{RoM} = \left(1 - \frac{2l_c}{l_b}\right)\tau_s + \left(\frac{2l_c}{l_b}\right)\tau_c \quad (1)$$

It is to be noted that the uniform curing cycle adopted for the tailored adhesives may not achieve the optimal mechanical properties. Hence, the failure strength of the tested joints should be benchmarked with two different values:

a) The design strength provided in the manufacturer data sheets (as in Table 1), different standards such as ASTM D1002, and MMM-A-132 are used by manufacturers to characterize the single lap shear strength of the polymeric adhesives. It denotes the maximum load-carrying capability of the adhesives under pure shear, cured with optimum conditions. The pristine joints S1 and S2 were only able to utilize 50% of their adhesive strength (τ_s). By tailoring with 20% hyperelastic adhesive. the AF3109 and EA9696 joint strength (AA2 and EA2) were increased to 76% and 62% of $\tau_{s\ AF3109}$ and $\tau_{s\ EA9696}$, repectively.

b) The theoretical upper limit calculated by RoM, equation 1- In this study, by tailoring with 20% hyperelastic adhesive, atleast 85% of $\tau_{RoM\ AF3109}$ and 70% of $\tau_{RoM\ EA9696}$ $\tau_{s\ AF3109}$ were attained by the AA2 joints and the EA2 joints.

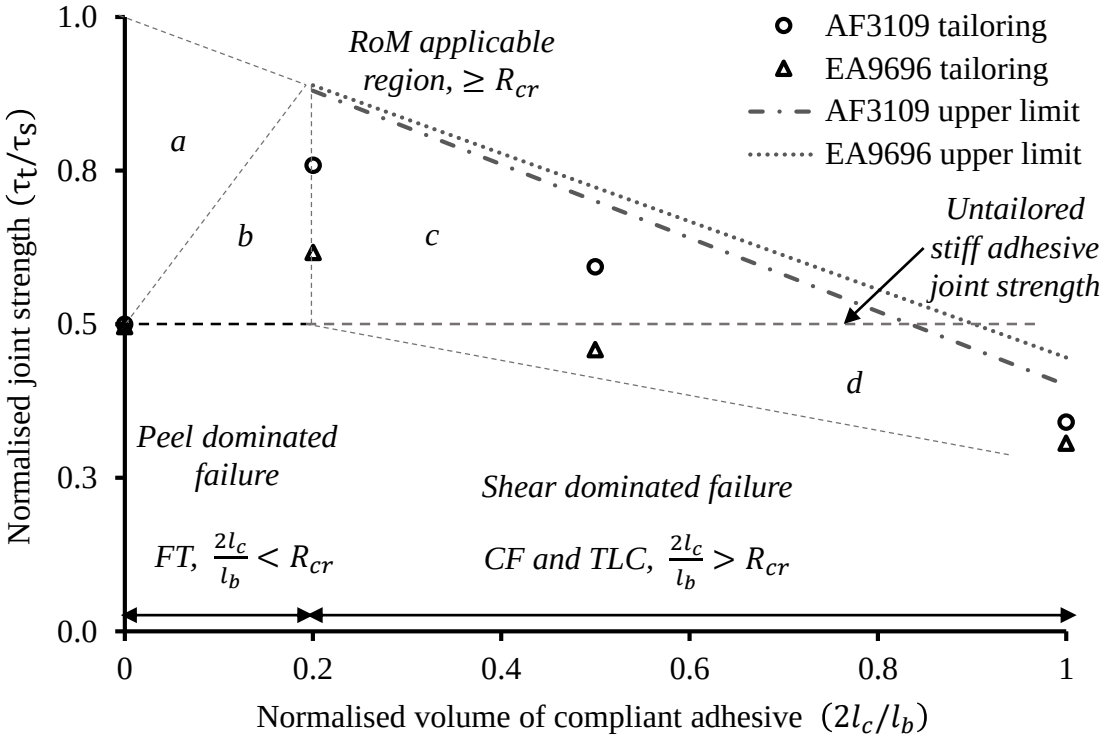

Figure 10. Failure mode map for the tailored adhesive joints in terms of normalised joint strength and compliant adhesive volume. The critical ratio, R_{cr} is defined by $\frac{2l_c}{l_b}$ at which the normalised joint strength is maximum.

The following observations were made with the help of the failure mode map.

i. when, $\frac{2l_c}{l_b} = 0$, the adhesive joint was entirely cured with the stiff adhesives and the composite joints failed by GFRP fibre-tear due to the edge peel stresses. By selecting adherends with higher interlaminar strength and stiffness; high strength- very low modulus adhesives; reducing the out-of-plane bending or using various techniques to reduce stress concentration, the maximum normalised joint strength can be attained. Hence, the RoM is not applicable in this region 'a'.

ii. when, $\frac{2l_c}{l_b} < R_{cr}$ (the critical ratio is around 0.2 for the current joint design) the edge peel stresses were reduced significantly (> 65%); however, the secondary tensile peak stress occurs at the compliant-stiff adhesive transition region, producing composite fibre-tear failure at the central stiff adhesive region whereas cohesive failure was observed in the compliant adhesive portion. Prediction of the composite fibre-tear failure load in terms of joint parameters, material properties for the SLJ is beyond the scope of this paper.

iii. when $\frac{2l_c}{l_b} = R_{cr}$, the optimized compliant adhesive proportion at which the joint was subjected to maximum failure load and failed by adhesive shearing mechanism. The dominant failure mode was noticed as COH failure in the stiff adhesive region.

iv. when $\frac{2l_c}{l_b} > R_{cr}$ (region 'c' and 'd'), the joints were bonded with a considerably higher proportion of the compliant adhesive where the joints were failed by shear mechanism and the failure strength was expected to decrease, befitting the RoM. If $\tau_c < \tau_s$, the joint strength is constrained by the compliant adhesive shear strength, leading to the final failure, at a lower load, like that of pristine joints (refer region 'c', AA1 joints). Further increasing the compliant adhesive can lead to the joint strength even lower than the stiff pristine joints, as seen in the region 'd' (EA1 joints) and interestingly, the failure mode is cohesive. Hence, it is not recommended to design the tailored joints with the compliant adhesive having very low design strength ($\tau_c \ll \tau_s$).

The design objective should be to reduce the composite adherend edge peel stresses and shifting the ply failure of composite into cohesive failure of adhesives in order to utilize the maximum design strength of the stiff adhesives (τ_s).

5 Conclusion

From the experimental testing and FE simulations of the GFRP SLJs with bi-adhesives, the following conclusions are being made :

1. The SLJ strength of the GFRP ductile epoxy adhesive joints exhibiting first-ply failure due to the peel stress dominance can be tailored with hyperelastic adhesives to improve the load-bearing capacity. Tailoring of the AF3109 and EA9696 based GFRP SLJs with 20% of hyperelastic adhesive improved the failure strength by 51.64% and 24.25%, respectively.
2. Finite element simulations consisting of EDP and Marlow models predicted the tensile behaviour of the bulk adhesives and SLJs, compared well with the experimental measurements. An increase in joint strength was attributed to the reduction in the edge peel stresses.
3. Failure analysis of the tested joints revealed that the failure mode changes from adherend fibre-tear failure to cohesive failure of adhesive due to tailoring through maximum utilization of the stiff adhesive design strength.
4. Manufacturing issues such as adhesives intermingling, same curing cycle and the unsymmetrical compliant adhesive length was observed and considering the low experimental scatter (a maximum of 3.6% in the EA2 joints), the failure strength was less influenced by these manufacturing deficiencies. The failure analysis showed complex fracture paths that were dominated by stiff adhesive.
5. Failure mode map suggests that the compliant adhesive proportion in the stiff adhesive bond line should be optimized to reduce the edge peel stresses as well as retaining the maximum proportion of stiff adhesive to resist the shear loads.

Acknowledgement

This work was conducted within the Rolls-Royce@NTU Corporate Lab under the project "ARMS 1.3 Repair of Composite Aero-engine Structures" with support from the Industry Alignment Fund (IAF) Singapore under the Corp Lab@University Scheme. Further Dr. S. Idapalapati thanks the financial support from MAE Research Incentive Grant. Authors thank Mr. V.S. Sridharan for experimental assistance and constructive suggestions and Mr. C. Gare Rern for his comments. Mr. V. Ravichandran acknowledges the internship provided through a project agreement between NTU Singapore and DSO National Laboratories through Dr. S. Idapalapati.

References

[1] Wang CH, Duong CN. Introduction and overview. Bonded Joints and Repairs to Composite Airframe Structures., Elsevier; 2016, p. 3–19. https://doi.org/10.1016/B978-0-12-417153-4.00001-3.

[2] Budhe S, Banea MD, de Barros S. Bonded repair of composite structures in aerospace application: a review on environmental issues. Appl Adhes Sci 2018;6. https://doi.org/10.1186/s40563-018-0104-5.

[3] da Silva LFM, Rodrigues TNSS, Figueiredo MA V., de Moura MFSF, Chousal JAG. Effect of Adhesive Type and Thickness on the Lap Shear Strength. J Adhes 2006;82:1091–115. https://doi.org/10.1080/00218460600948511.

[4] Tang JH, Sridhar I, Srikanth N. Static and fatigue failure analysis of adhesively bonded thick composite single lap joints. Compos Sci Technol 2013;86:18–25. https://doi.org/10.1016/j.compscitech.2013.06.018.

[5] Banea MD, Rosioara M, Carbas RJC, da Silva LFM. Multi-material adhesive joints for automotive industry. Compos Part B Eng 2018;151:71–7. https://doi.org/10.1016/j.compositesb.2018.06.009.

[6] Adams RD. Strength predictions for lap joints, especially with composite adherends. A review. J Adhes 1989;30:219–42. https://doi.org/10.1080/00218468908048207.

[7] Fitton MD, Broughton JG. Variable modulus adhesives: an approach to optimised joint performance. Int J Adhes Adhes 2005;25:329–36. https://doi.org/10.1016/j.ijadhadh.2004.08.002.

[8] F M da Silva L, D Adams R. Techniques to reduce the peel stresses in adhesive joints with composites. Int J Adhes Adhes 2007;27:227–35. https://doi.org/10.1016/j.ijadhadh.2006.04.001.

[9] Shang X, Marques EAS, Machado JJM, Carbas RJC, Jiang D, da Silva LFM. Review on techniques to improve the strength of adhesive joints with composite adherends.

Compos Part B Eng 2019;177:107363. https://doi.org/10.1016/j.compositesb.2019.107363.

[10] Boss JN, Ganesh VK, Lim CT. Modulus grading versus geometrical grading of composite adherends in single-lap bonded joints. Compos Struct 2003;62:113–21. https://doi.org/10.1016/S0263-8223(03)00097-7.

[11] da Silva LFM, Lopes MJCQ. Joint strength optimization by the mixed-adhesive technique. Int J Adhes Adhes 2009;29:509–14. https://doi.org/10.1016/j.ijadhadh.2008.09.009.

[12] Marques EAS, Da Silva LFM, Flaviani M. Testing and simulation of mixed adhesive joints for aerospace applications. Compos Part B Eng 2015;74:123–30. https://doi.org/10.1016/j.compositesb.2015.01.005.

[13] Durodola JF. Functionally graded adhesive joints – A review and prospects. Int J Adhes Adhes 2017;76:83–9. https://doi.org/10.1016/j.ijadhadh.2017.02.008.

[14] Kumar S, Wardle BL, Arif MF. Strength and Performance Enhancement of Bonded Joints by Spatial Tailoring of Adhesive Compliance via 3D Printing. ACS Appl Mater Interfaces 2017;9:884–91. https://doi.org/10.1021/acsami.6b13038.

[15] Stapleton SE, Waas AM, Arnold SM. Functionally graded adhesives for composite joints. Int J Adhes Adhes 2012;35:36–49. https://doi.org/10.1016/j.ijadhadh.2011.11.010.

[16] Das Neves PJC, Da Silva LFM, Adams RD. Analysis of mixed adhesive bonded joints part I: Theoretical formulation. J Adhes Sci Technol 2009;23:1–34. https://doi.org/10.1163/156856108X336026.

[17] das Neves PJC, da Silva LFM, Adams RD. Analysis of Mixed Adhesive Bonded Joints Part II: Parametric Study. J Adhes Sci Technol 2009;23:35–61. https://doi.org/10.1163/156856108X336035.

[18] Stein N, Weißgraeber P, Becker W. Stress solution for functionally graded adhesive joints. Int J Solids Struct 2016;97–98:300–11. https://doi.org/10.1016/j.ijsolstr.2016.07.019.

[19] Kumar S. Analysis of tubular adhesive joints with a functionally modulus graded bondline subjected to axial loads. Int J Adhes Adhes 2009;29:785–95. https://doi.org/10.1016/j.ijadhadh.2009.06.006.

[20] Galvez P, Noda NA, Takaki R, Sano Y, Miyazaki T, Abenojar J, et al. Intensity of singular stress field (ISSF) variation as a function of the Young's modulus in single lap adhesive joints. Int J Adhes Adhes 2019;95:102418. https://doi.org/10.1016/j.ijadhadh.2019.102418.

[21] Bedon C, Machalická K, Eliášová M, Vokáč M. Numerical modelling of adhesive connections including cohesive damage. Challenging Glas 6 Conf Archit Struct Appl Glas CGC 2018 - Proc 2018:309–20. https://doi.org/10.7480/cgc.6.2155.

[22] García JA, Chiminelli A, García B, Lizaranzu M, Jiménez MA. Characterization and material model definition of toughened adhesives for finite element analysis. Int J Adhes Adhes 2011;31:182–92. https://doi.org/10.1016/j.ijadhadh.2010.12.006.

[23] Özer H, Öz Ö. The use of the exponential Drucker-Prager material model for defining the failure loads of the mono and bi-adhesive joints. Int J Adhes Adhes 2017;76:17–29. https://doi.org/10.1016/j.ijadhadh.2017.02.005.

[24] Xu B. Fracture Mechanisms and Failure Criteria of Adhesive Joints and Toughened Epoxy Adhesives. Queen Mary University of London, 2010.

[25] Staudt Y, Odenbreit C, Schneider J. Failure behaviour of silicone adhesive in bonded connections with simple geometry. Int J Adhes Adhes 2018;82:126–38. https://doi.org/10.1016/j.ijadhadh.2017.12.015.

[26] 3M™ Scotch-Weld™ Structural Adhesive Film AF32. Safety Data Sheet, 2018.

[27] 3M™ Scotch-Weld™ Structural Adhesive Film AF 3109-2. Technical Data Sheet, 2002.

[28] Hysol® EA 9696 Epoxy Film Adhesive Technical Data Sheet.

[29] 3M™ Scotch-Weld™ Structural Adhesive Film AF32. Technical Data Sheet

[30] American Society for Testing Materials (ASTM). Standard Test Method for Tensile Properties of Plastics. Designation: ASTM D638-14, 2014.

[31] Rajaneesh A, Sridhar I, Rajendran S. Failure mode maps for circular composite sandwich plates under bending. Int J Mech Sci 2014;83:184–95. doi:10.1016/j.ijmecsci.2014.03.029.

[32] Firmo F, Jordão S, Costa Neves L, Bedon C. The effect of adhesive joints on the performance of hybrid steel-glass beams – An analytical and experimental study. Challenging Glas Conf Proc - Challenging Glas 5 Conf Archit Struct Appl Glas CGC 2016 2016:171–86.

[33] Smith LV. Durability of Bonded Aircraft Structure. FAA Annu Tech Rev Meet 2016.

[34] Mohapatra PC, Scarborough H, Smith LV. A comparison of hydrostatic and plastic yield criteria for a toughened adhesive. Int SAMPE Tech Conf 2016;2016-Janua..

[35] Kumar S, Pandey PC. Behaviour of Bi-adhesive Joints. J Adhes Sci Technol 2010;24:1251–81. https://doi.org/10.1163/016942409X12561252291982.

[36] D5573-99(2005), “Standard Practice for Classifying Failure Mode in Fibre-Reinforced-Plastic (FRP),” ASTM B. Stand., vol. 99, no. Reapproved, pp. 1–18, 2005, doi: 10.1520/D5573-99R12.2.

[37] Tsai MY, Morton J. An evaluation of analytical and numerical solutions to the single-lap joint. Int J Solids Struct 1994;31:2537–63. https://doi.org/10.1016/0020-7683(94)90036-1.

[38] ABAQUS® Documentation v.6.14. Dassult Systems 2014.

[39] Dean G, Crocker L, Read B, Wright L. Prediction of deformation and failure of rubber-toughened adhesive joints. Int J Adhes Adhes 2004;24:295–306. https://doi.org/10.1016/j.ijadhadh.2003.08.002.

Appendix A- Exponential Drucker-Prager (EDP) model

The yield behaviour of tough ductile epoxy adhesive is a function of hydrostatic and von-Mises effective or equivalent stresses and is expressed as [38]:

$$aq^b = p + p_t \quad \text{(A1)}$$

where p, q and p_t are hydrostatic stress, equivalent stress, and hardening parameter representing hydrostatic tensile strength. *'a'* and *'b'* are the plastic strain independent adhesive material parameters: b = 2 fits well with the experimental data for epoxy adhesives [39]. 'a' in terms of adhesive's hydrostatic stress sensitivity parameter (λ) (which is a ratio of the compressive yield stress (σ_C) to the tensile yield stress (σ_T)) can be expressed as,

$$a = \frac{1}{3\,(\lambda-1)\sigma_T} \quad \text{(A2)}$$

The hardening parameter (p_t) is given by,

$$p_t = \frac{\lambda\sigma_T}{3\,(\lambda-1)} \quad \text{(A3)}$$

The dilation angle or flow parameter (ψ) characterising the plastic flow in terms of plastic Poisson's ratio (ϑ^p) is expressed as,

$$\tan\psi = \frac{3(1-2\vartheta^p)}{2(1+\vartheta^p)} \quad \text{(A4)}$$